

TIME-FREQUENCY AND ISAR CHARACTERISTICS OF WIND TURBINES WITH HIGHER ORDER MOTIONS

Aale Naqvi* and **Hao Ling**

Department of Electrical and Computer Engineering, The University of Texas at Austin, Austin, TX 78712-1084, USA

Abstract—Radar features from higher order motions of a wind turbine undergoing rotation are studied. Mathematical models for the motions are proposed and used to simulate the joint time-frequency (JTF) and inverse synthetic radar aperture (ISAR) characteristics of the motions. The motions are studied for an isolated turbine as well as for a turbine rotating above a ground. Selected motions are corroborated by laboratory model measurements.

1. INTRODUCTION

Interest in wind power as a viable form of renewal energy has resulted in a significant increase in the number and size of wind farms in the past several years. The increase in the number of wind farms has raised serious concerns in the radar community due to the radar clutter produced by wind turbines. The rotation of the turbine blades leads to unwanted Doppler clutter that can adversely affect the performance of radars for weather, air traffic control, and long-range surveillance [1–7]. Understanding the clutter features in detail is a necessary step towards developing mitigation techniques. A number of previous studies have reported the Doppler features of turbines in isolated as well as complex settings [8–16].

While the radar Doppler features due to turbine blades undergoing a simple rotation motion have been well examined, higher order motions such as structural flexing and vibration may also be present under dynamic operating conditions. It is important to understand the various radar features that can arise due to these motions. In this paper, we simulate the radar features that may arise due to various types of higher order turbine motions and examine their time-varying Doppler characteristics. The motions examined include blade

Received 9 October 2013, Accepted 31 October 2013, Scheduled 8 November 2013

* Corresponding author: Aale Naqvi (aalenqvi@yahoo.com).

vibrations, blade flexing, and tower vibrations. The resulting Doppler features are then examined in the joint time-frequency (JTF) plane and inverse synthetic aperture radar (ISAR) imagery.

This paper is organized as follows. In Section 2, we propose motion models used to simulate the motions. In Section 3, we use the proposed models to examine the JTF characteristics of a free-standing turbine. The short-time Fourier transform (STFT) is used to obtain the JTF representation. Next, we extend our analysis of the higher order motions to the ISAR image plane in Section 4. This broadens the motion analysis to include the range dimension in addition to the Doppler characteristics of turbines. In Section 5, the ISAR analysis is extended to take into account ground effects. Selected simulated motions are corroborated by laboratory model measurements in Sections 3–5. Finally, Section 6 provides the conclusions of the presented work.

2. MOTION MODELS

In this section, mathematical models to simulate the turbine motions are proposed. The motion models are constructed using a simplified point-scatterer basis. Point scatterer basis is a simple and approximate way to model a radar target [17, 18]. In the particular case of a turbine, each blade of the turbine can be modeled as a set of closely spaced point scatterers. Here we adopt the same approach and extend it to incorporate higher-order turbine motions. Edge-on incidence of the radar wave is assumed as shown in Figure 1, as it produces the maximum Doppler extent, and thus the worst-case Doppler clutter. Using the point scatterer approach, the signal from turbine blades can be modeled by Equation (1):

$$\phi(t) = \sum_{l=0}^2 \sum_{m=1}^M A_m \exp \left(-2jk \sqrt{((R - X_m)^2 + Y_m^2)} \right) \quad (1)$$

where A_m is the reflectivity strength of each point scatterer and the phase of the exponential represents the two-way path length of the wave from the radar to the turbine and back towards the radar. The variables in the exponential are as follows: k is the free-space propagation constant; R is the position of the radar relative to the hub of the blades along the x -axis; X_m and Y_m are respectively the x and y coordinates of each point scatterer. The inner summation controlled by the subscript, m , controls the position and the strength of each point scatterer along a single blade while the outer summation, over l , controls the angular spacing between the blades, which is $2\pi/3$.

The various motions of the turbine can be modeled by choosing appropriate expression for X_m and Y_m . For uniform circular turbine motion, X_m and Y_m can be written as:

$$X_m = R_m \cos(\omega t + \theta_o + 2\pi l/3) \tag{2}$$

and

$$Y_m = R_m \sin(\omega t + \theta_o + 2\pi l/3) \tag{3}$$

where R_m is the magnitude of the distance of a point scatterer from the hub of the blades.

Four types of higher order motions that may exist on top of the uniform rotation motion of the blades are considered. The higher order motions include in-plane vibrations, out-of-plane vibrations, blade flexing, and tower vibrations. The five motions described are pictorially represented in Figure 1. Figure 1(a) represents the turbine blades moving in a uniform circular motion. Figures 1(b)–(e) respectively are the blades undergoing additional in-plane vibration, out-of-plane vibration, blade flexing, and tower vibration motions in addition to the circular motion of the turbine.

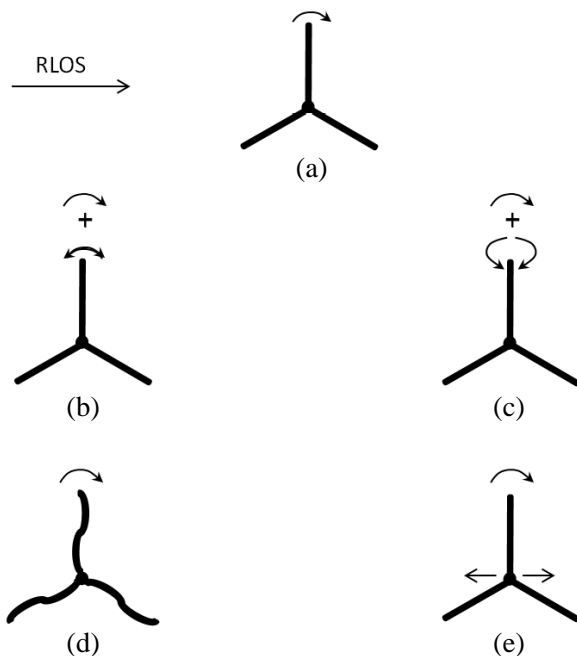


Figure 1. Pictorial representation of the blade motions. (a) Uniform rotation motion. (b) In-plane vibrations. (c) Out-of-plane vibrations. (d) Blade flexing. (e) Tower vibration.

We refer to the blade vibrations that may occur within the plane of the rotating blades as in-plane vibrations. The proposed motion model incorporating in-plane vibrations is described by Equations (4) and (5):

$$X_m = R_m \cos(\omega t + \theta_o + 2\pi l/3 + \Delta\theta \cos(\omega_{vib} t)) \quad (4)$$

and

$$Y_m = R_m \sin(\omega t + \theta_o + 2\pi l/3 + \Delta\theta \cos(\omega_{vib} t)) \quad (5)$$

where $\Delta\theta$ is the angular amplitude of the vibration and ω_{vib} is the angular frequency of the in-plane vibrations.

A motion model of out-of-plane vibrations is shown in Equations (6) and (7):

$$X_m = R_m \cos(\omega t + \theta_o + 2\pi l/3) \sin(\pi/2 + \Delta\phi \cos(\omega_{vib} t)) \quad (6)$$

and

$$Y_m = R_m \sin(\omega t + \theta_o + 2\pi l/3) \sin(\pi/2 + \Delta\phi \cos(\omega_{vib} t)) \quad (7)$$

where the out-of-plane motion along the z -direction has been projected into the xy -plane by the second sine term. The z -displacement can be ignored since it does not result in any Doppler shift detected by the radar. The argument of the second term models out-of-plane vibrations while the additional $\pi/2$ phase keeps the motion centered about the xy -plane.

This model can also incorporate blade flexing motion. It can be accomplished by varying the angular position of each point scatterer. Curvature can be introduced into the blade by appropriately assigning values of the starting angle, θ_m , to each point scatterer and varying the values appropriately with time. A model of blade flexing is given by Equations (8) and (9):

$$X_m = R_m \cos(\omega t + \theta_o + \theta_{amp} \sin(\omega_f t + \theta_m) + 2\pi l/3) \quad (8)$$

and

$$Y_m = R_m \sin(\omega t + \theta_o + \theta_{amp} \sin(\omega_f t + \theta_m) + 2\pi l/3) \quad (9)$$

where ω_f is the flexing frequency of the blades, and θ_{amp} controls the amplitude of the flexing.

Finally, tower vibrations can be incorporated into our model by varying the range of the turbine relative to the radar, i.e., the ' R ' that appears in Equation (1). The ' R ' can be rewritten as:

$$R = R_o + A_t \sin(\omega_t t) \quad (10)$$

where A_t and ω_t respectively are the amplitude and the frequency of the tower motion. Although a physical tower is not present in the model, we assume the dominant Doppler contribution will come from the turbine hub — the farthest point from the base of the tower.

3. TURBINE JTF CHARACTERISTICS

Having proposed the analytical higher-order motion models, their resulting JTF signatures are presented in this section. In the simulations, the blade length is set to 34 m. The spacing between the point scatterers is set to $\lambda/5$ to ensure that the simulated results resemble the real returns from a turbine. The blades are assumed to be rotating at 12 rpm. The radar frequency is at 1.5 GHz, which is typical of long-range surveillance radar. The complex backscattered data as a function of time are processed using the STFT to obtain the spectrogram. A time window of 0.3 second is used in the STFT and a Gaussian window is applied before the Fourier transform. The parameters for the higher order motion are chosen to emphasize and clearly display the new features that may arise based on the proposed models.

Figure 2 shows a set of figures demonstrating the JTF characteristics using the point scatterer model. Figure 2(a) is the spectrogram for uniformly rotating blades acquired using Equations (2) and (3). The most prominent features seen are the blade flashes that occur when the blade is perpendicular to the radar line-of-sight. The blade flashes are positive when a blade is approaching the radar and are negative when it is receding away. The blade flashes occur after every 60 degree rotational motion of the blades. The flashes are enveloped by sinusoidal “tip halos” that arise due to tip diffraction. The tip halos are sinusoidal due to the circular motion of the blades. The point scatterer model successfully captures the key Doppler features of the blade motion seen in in-situ measurements reported in [10].

Figure 2(b) is the spectrogram with in-plane vibrations introduced. In this case, the vibration amplitude, $\Delta\theta$ and ω_{vib} appearing in Equations (4) and (5) are set to 0.8 degree and 33 rpm respectively. With in-plane vibrations, the extra motion is evident in several forms. The extra motion is due to $\Delta\theta$ and ω_{vib} that effectively increase or decrease the radial velocity of the blades. The tip halo loses its perfectly sinusoidal shape and is distorted since the radial velocity of the blade relative to the radar varies at various times along the blades' motion. Since the radial velocity of the blade changes, the maximum Doppler of the tip-halos also varies and may be lower or higher than the case without any vibration depending on whether the blade is increasing or decreasing in velocity due to the vibrations. Furthermore, although not immediately evident in the spectrogram, the angular spacing between adjacent flashes is not exactly 60 degrees. This difference is also attributed to the time-varying vibrational changes that the blades undergo.

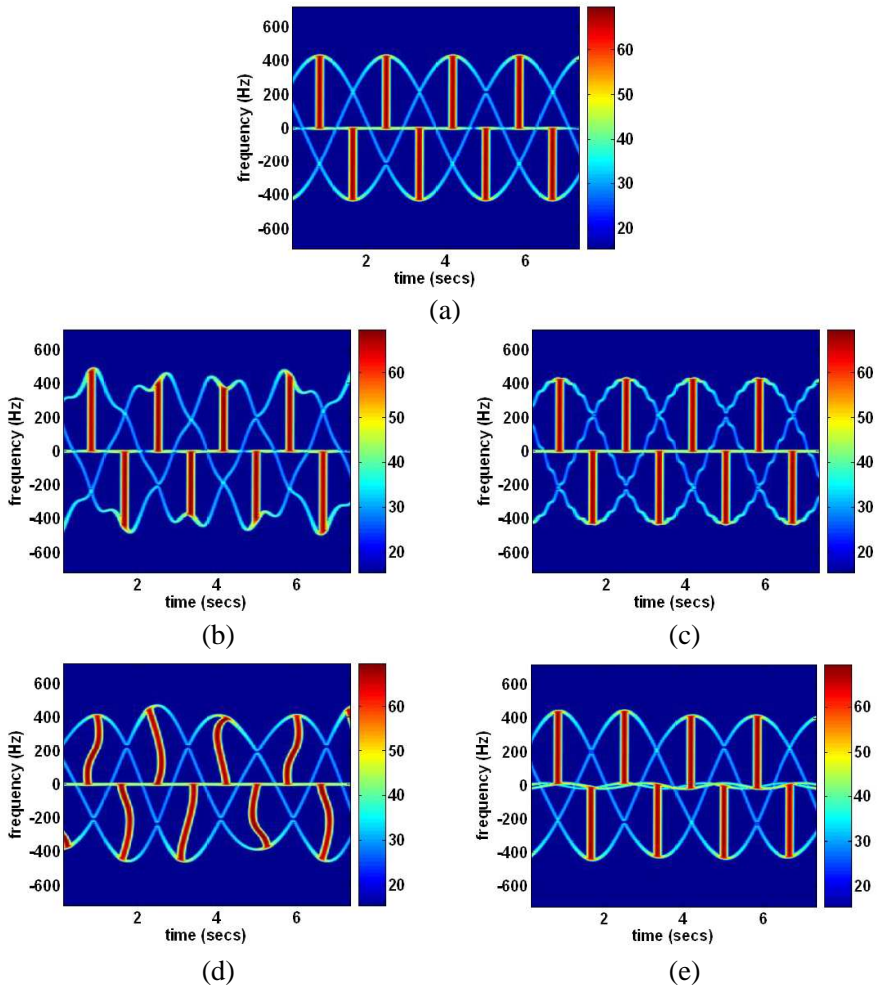


Figure 2. Point scatterer simulated JTF characteristics of the turbine motion. (a) Uniform circular motion. (b) In-plane vibrations. (c) Out of plane vibrations. (d) Blade flexing. (e) Tower vibrations.

Figure 2(c) incorporates out-of-plane vibrational motion into the uniform circular motion of the turbine. The $\Delta\phi$ and ω_{vib} in Equations (6) and (7) are set to 5 degrees and 50 rpm respectively. The spectrogram shows clear tip distortion. The tip distortion has a unique signature and is rather different from the tip distortion observed for in-plane vibrations. However, the flash Doppler and spacing remains uniform.

In Figure 2(d), the blades are assumed to undergo flexing motion. The flexing frequency, ω_f , in Equations (8) and (9) is set to 12 rpm while θ_{amp} is set to 0.1 degree. The most conspicuous feature of the spectrogram is the curved blade flashes. The curved flashes result because different parts of the blade are perpendicular to the radar at different times and the nature of the flexing manifests itself in the curvature of the flashes. The flexing motion also causes variations in maximum Doppler of the tip halos in the spectrogram.

Finally, Figure 2(e) shows the JTF characteristics of turbine motion with the tower vibrating. Here, the vibration amplitude is set to 1 m which corresponds to a maximum angular displacement of 0.96 degree of the hub for a 60 m long tower. The vibrating frequency is set to 30 rpm. The vibration of the tower adds a Doppler shift to the DC line and in this case, the shift is sinusoidal as modeled in Equation (10). The blade flashes and tip halos are observed to ride on the sinusoid from the tower motion, which varies the effective radial velocity of the blades relative to the radar wave.

Having modeled and simulated the JTF characteristics of the various turbine motions, we carry out laboratory model measurements to corroborate the simulations. Figure 3(a) is a photo of the measurement set-up. The measurements were carried out as follows. A vector network analyzer (*Agilent N5230A*) was used to collect measurement data in continuous wave (CW) mode at 11 GHz. The turbine comprises a 3-arm wire model with 60 cm long blades and a wire radius of 1.2 mm. Notice that our model is about 60 times smaller than the simulation while the frequency is scaled up only by a factor of 8. This is due to the limitation of our measurement equipment. The data were collected for 65.5 seconds, which corresponds to one rotational period of our turn-table, while the sampling rate was set at 22 Hz. S_{11} parameters were collected from a rotating turbine using a horn antenna placed 2.2 m from the center of the blades. Since the radar was located within the near field of the turbine, a near-field to far-field transform algorithm discussed in [19] was applied to the data to eliminate near-field effects. Background subtraction was performed to reduce the effects of reflection within the horn, which gave rise to a very strong zero-Doppler component. The complex scattering data versus time were processed using the STFT. A time window of 5-second was used to process our results.

The JTF results of the measurement data are shown in Figure 3. Figure 3(b) shows the spectrogram from a uniformly rotating turbine. We observe the blade flashes and the tip halos described earlier. Figure 3(c) shows the spectrogram resulting from “simulated” in-plane vibrations. In order to acquire Figure 3(c), the data were re-sampled

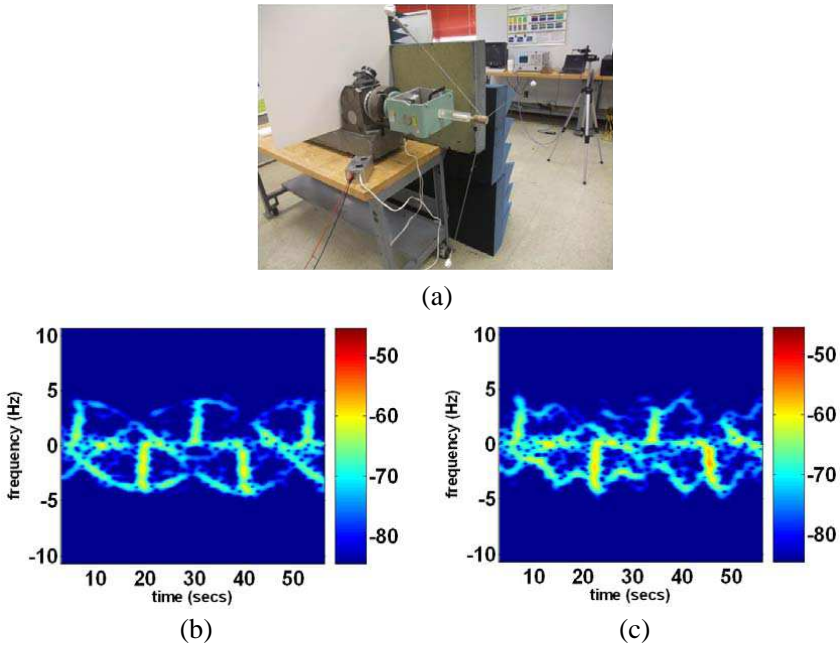


Figure 3. Measurement set-up and results. (a) The set-up. (b) Spectrogram of uniformly rotating turbine. (c) Spectrogram with in-plane vibrations injected.

from Figure 3(a) at the desired angles dictated by the motion models in Equations (4) and (5). In order to resample the data, we first sinc-interpolate our signal to increase the sampling rate. Next, we set $\Delta\theta$ and ω_{vib} to 1.5 degrees and $8/66 * 2 * \pi$, respectively, to acquire the measured data under the assumed motion. Clearly seen in Figure 3(c) are the tip distortion and non-uniform max flash Doppler that are similar in nature to those seen in Figure 2(b). Also, due to the difference in the speeds of the two cases, Figure 3(c) only contains four while Figure 3(b) contains five flashes.

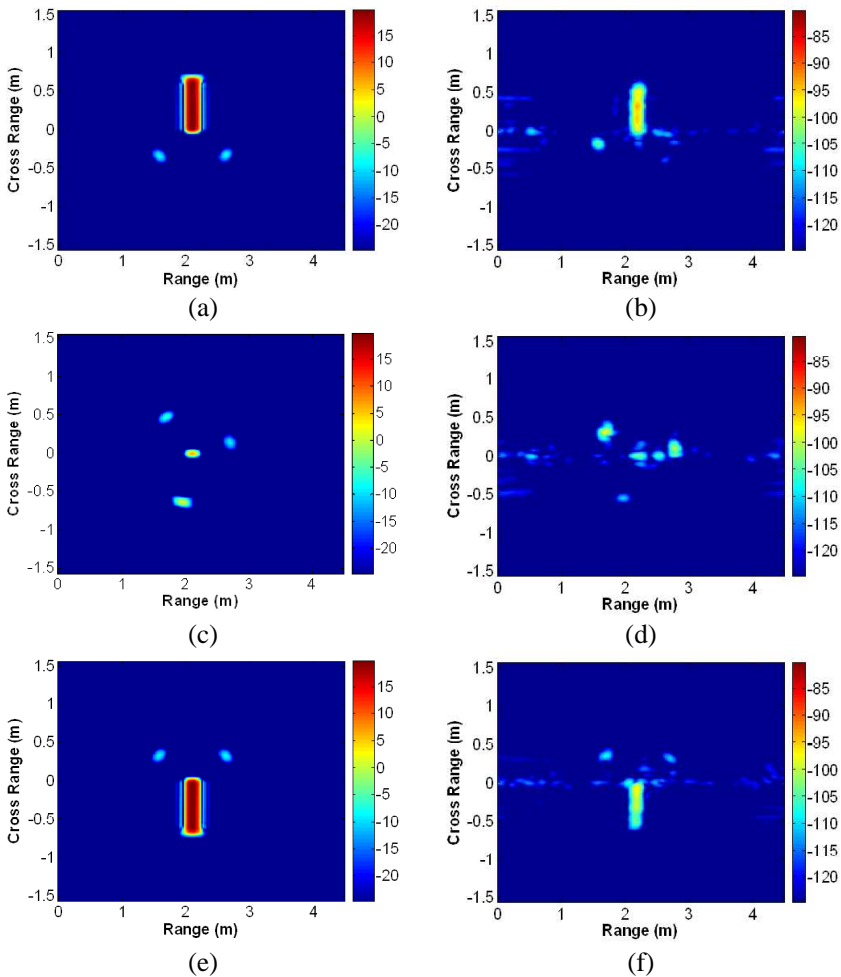
4. TURBINE ISAR CHARACTERISTICS

The JTF analysis in the last section allows us to observe the time-varying Doppler characteristics of the turbine motion. However, it does not provide down-range information of the turbine structure. In this section, we introduce the range dimension into our feature analysis and study the turbine features in the (range)-(cross range) plane, or

its ISAR image. The results are presented as a single composite image of all the images acquired in the course of rotation of turbine blades.

4.1. Composite ISAR Images — Simulation and Measurement

In this section, we focus first on a turbine undergoing regular rotation to illustrate the process of forming a composite ISAR image. Simulations and measurements were carried out for a turbine model with 60 cm blades. To form an ISAR image, backscattered data over a finite frequency bandwidth and target rotation angles are needed.



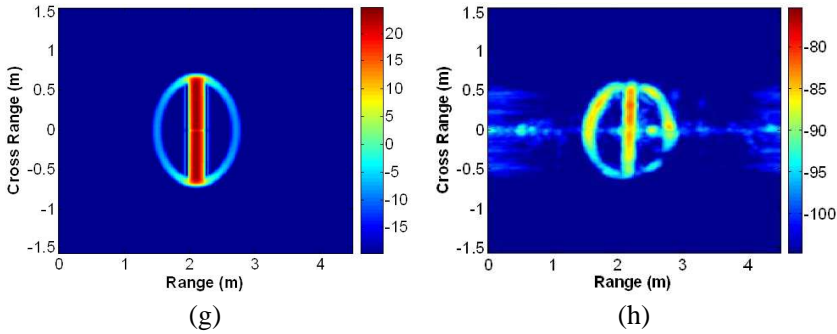


Figure 4. ISAR images of turbine at various blade angular positions. (a), (c), and (e) are simulated using point scatterer model. (a) Positive flash. (c) Blades in a non-flashing position. (e) Negative flash. (g) Composite image. (b), (d), (f), and (h) are corresponding measured results.

In the measurements, we swept over a range of frequencies from 10–12 GHz in increments of 33.3 MHz. The turbine motion was sampled at every 0.5 degree of rotation. Each image of the turbine was formed by processing 24 degrees of data. The point scatterer basis was modified to take into accounts the above parameters. The simulations were performed in the far-field while the near-field to far-field algorithm [19] was used to eliminate near-field effects in the measurements.

First, the ISAR images of a single turbine at selected positions are presented. Figure 4 shows the simulated and measured ISAR images of a turbine at three different angular positions. Figure 4(a) shows a simulated image of a turbine for the case of a positive flash. The other two blade tips are observed as the two points seen in the figure. Figure 4(c) shows a snap shot of the blades for the case when none of them are in a flashing position and we only observe the tips of each blade. Figure 4(e) shows the case of a negative flash. Figures 4(b), (d), and (f) are the corresponding measured results corroborating the simulations. For the measurements, the actual collected data result in images with a cross range between -0.7 m and 0.7 m. The images are zero-padded in cross range for an easier comparison with the simulations. Figures 4(g) and (h) are the corresponding composite ISAR images, which are formed as follows. First, a single image is generated as described above. Subsequently, the imaging window is slid by 2 degrees to obtain a sequence of images of the turbine as it rotates until both a positive and a negative flash are captured in the image. Finally, the images are summed in intensity to obtain a

complete composite ISAR image of the blades. Other than the intensity difference, the key features in the simulation and measurement images agree.

4.2. Composite ISAR Images with Higher Order Motions

Having demonstrated how single-snapshot images can be combined to form a meaningful composite ISAR image of a uniformly rotating turbine, we shall use this representation to study different higher order motions for a full size turbine. The size of the turbine blade is the same as that in Section 3, or 34 m. In order to obtain ISAR for full size turbines, the point scatterer basis is modified to sweep over a bandwidth of 75 MHz with the center frequency set at 1.5 GHz at increments of 1.25 MHz. The simulated turbine motion is sampled at every 0.05 degree of rotation. Each image of the turbine is formed by processing 3 degrees of data. Subsequently, the imaging window is slid 1.5 degrees to obtain the image sequence of the turbine as it rotates until both a positive and a negative flash is captured in the image.

Figure 5(a) shows the ISAR for a uniformly rotating turbine. As seen previously, the key features in the image are the positive and negative blade flashes and the circular tip centered between the flashes. The tip halos seen in the JTF plane become circle in the ISAR plane due to the circular motion of the blades. Figure 5(b) is the ISAR composite image for the case where the blades undergo in-plane vibrations. It is observed that the tip wobbles in the two-dimensional ISAR plane and the three distinct tip halo tracks are observed corresponding to each blade. Figure 5(c) shows the case for out-of-plane vibrations. The flashing behavior remains identical to the case without vibrations. Also, the slightly jagged nature of the tip vibrations is clearly seen for this case. Figure 5(d) is the case when the blades flex during rotation. The flexing of the blades is evident in the curvature of the positive and negative flashes. Also, the tip is observed to be slightly distorted. The weaker flashing strength for the cases of 5(c) and (d) is due to the variation in the spread of the flash energy in range and cross range. Figure 5(e) is the case for tower vibrations. This motion is observed in the range dimension in the form of shifted blade flashes. Also, due to the motion of the tower, the tip is distorted.

In order to provide some validation of the simulated phenomenology, we again use a re-sampling of the measured data from the laboratory model to emulate the effect of in-plane vibration. Figure 6(b) shows the ISAR image resulting from simulated in-plane vibrations. In order to acquire Figure 6(b), the data were re-sampled from Figure 6(a) (note that Figure 6(a) is the same as Figure 4(h)). The data

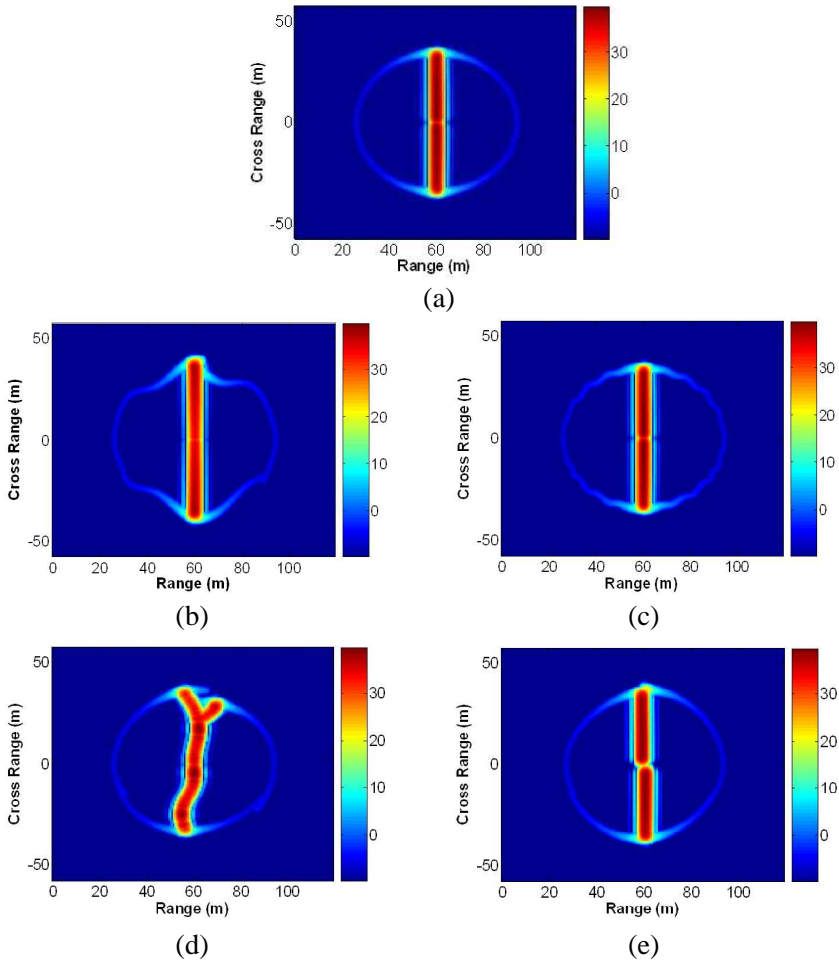


Figure 5. Composite ISAR images of turbine. (a) Uniform circular rotation. (b) In-plane vibrations. (c) Out-of-plane vibrations. (d) Blade flexing. (e) Tower vibrations.

were re-sampled using the motion models in Equations (4) and (5). We set $\Delta\theta$ and ω_{vib} to 1.5 degrees and $8/66 * 2 * \pi$, respectively, as was done for the data shown in Figure 3(b). We observe that the tip trace in Figure 6(b) shows distortion in the ISAR plane. This is consistent with the findings from Figure 5(b).

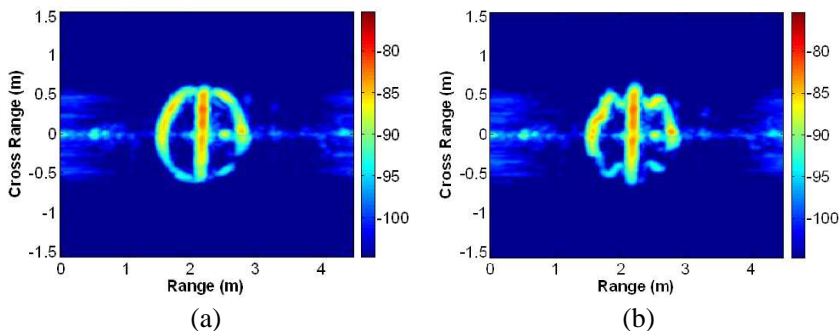


Figure 6. Measured composite ISAR image. (a) Uniformly rotating turbine. (b) With in-plane vibrations injected.

5. TURBINE ISAR CHARACTERISTICS IN THE PRESENCE OF GROUND

Real turbines are located on top of ground, and therefore turbine-ground interactions exist. In this section, the ISAR characteristics of the turbine blades rotating above an infinite ground plane are studied. With the presence of ground, additional returns due to single and double ground bounces are expected. The detailed physics of the ground interactions was studied and detailed in [16]. Single and double ground bounces are incorporated in our model by using image theory [20] and appropriately accounting for the wave's travel distance for each interaction as the blades rotate. The incident elevation angle is set to 20 degrees for the ground studies. The center frequency and the bandwidth width is kept the same as in Section 4, however, the frequency sampling is decreased to 937.5 kHz to obtain a larger range window. The blade height is set to 60 m above the ground. Again, we focus on the blade contribution only.

The case of a stationary ground is analyzed first. Figure 7 are the simulated ISAR images for each motion. Figure 7(a) shows the case of uniformly rotating blades in the presence of ground. We notice that in addition to the direct return, two additional sets of flashes encompassed by a circular tip halo are present. The first range-delayed return is due to the single ground-bounce effect. The second range-delayed return is due to the double ground-bounce effect. Figures 7(b), (c), (d), and (e) respectively are the cases of in-plane vibrations, out-of-plane vibrations, blade flexing, and tower vibrations. We notice that the key difference in presence of ground is that the single and ground bounce interactions are added to the image while the vibrational motions in

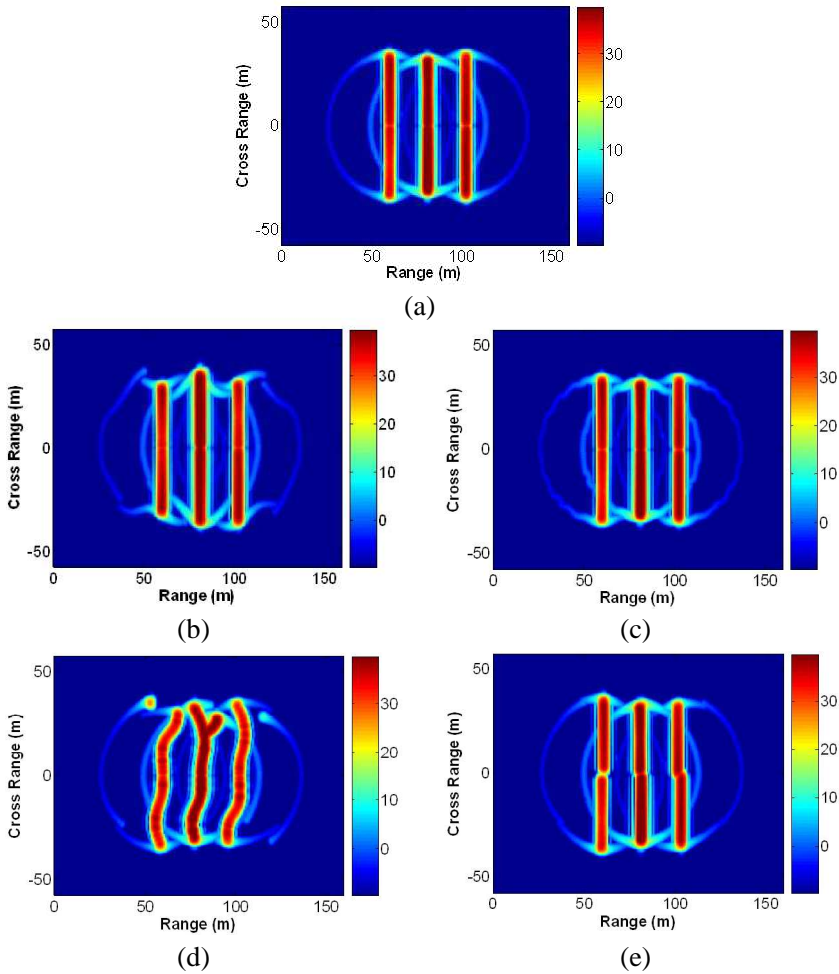


Figure 7. Composite ISAR images of turbine in the presence of ground. (a) Uniform circular roation. (b) In-plane vibrations. (c) Out-of-plane vibrations. (d) Blade flexing. (e) Tower vibrations.

each interaction manifest themselves in very similar manner as for the case of no ground.

Experimental corroboration of the ISAR in the presence of ground for the case of turbine uniformly blades as well as the blades that undergo in-plane vibrations is provided by Figure 8. A large metal ground plane was added to the scene during the measurement. As with earlier measurements, we processed our raw data through a near-

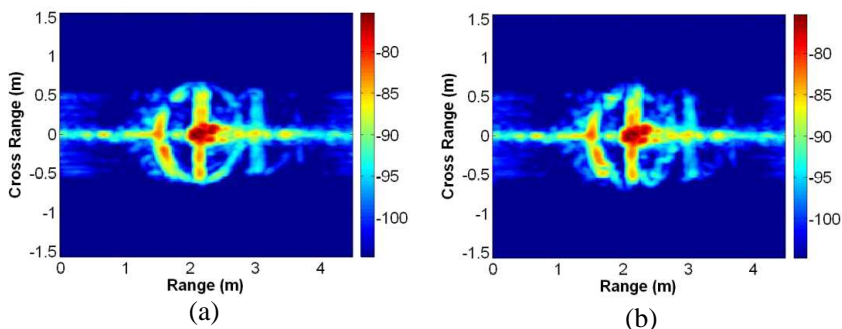


Figure 8. Measured composite ISAR images of turbine in presence of ground. (a) Uniform circular rotation. (b) In-plane vibrations injected.

field to far-field transform algorithm to eliminate the phase distortion in the near-field measurement. However, no amplitude correction was made to account for near-field effects. The direct and single ground bounce returns are observed to be present in the measured results. The single ground bounce is weaker in return because the wave decays in strength due to the larger space loss. Space loss is also the reason for the very faint double ground bounce return. In the earlier simulation results, space loss was not included since the radar was assumed to be in the far field of the turbine. Figure 8(a) shows the case of uniform rotation of the blades. Figure 8(b) shows the case with injected in-plane vibrations. We observe the familiar features for the cases of direct and single ground bounce returns.

6. CONCLUSION

The radar scattering characteristics from higher order motions of a wind turbine undergoing rotation have been modeled using a simplified point scatterer basis. The higher order motions studied included in-plane vibrations, out-of-plane vibrations, blade flexing, and tower vibrations. The models were subsequently used to simulate the JTF and ISAR characteristics of these motions. The cases of an isolated turbine and a turbine in the presence of ground were simulated. Image theory was used to incorporate ground effects into our point scatterer basis. Selected simulation cases were corroborated by laboratory model measurements. JTF analysis showed the time-varying Doppler characteristics of the higher order motions while ISAR analysis extended the study to incorporate the down range motion information. It was observed that various higher order motions are manifested as unique radar features. Therefore, it may be feasible to

use these observed radar features to identify motion irregularities in operating turbines. This could open up the possibility of using radar to monitor the structural health of large wind turbines.

ACKNOWLEDGMENT

This work was supported by the National Science Foundation under Grant ECCS-1232152, and in part by the Department of Energy under Grant DE-EE0005380.

REFERENCES

1. "Special evaluation report to assess effect of wind turbine farm on air route surveillance radar-4 at King Mountain, Texas," USAF 84 RADES & FAA, May 30, 2002.
2. "The effects of wind turbine farms on ATC radars," Air Warfare Center, Royal Air Force, UK, May 10, 2005.
3. "Further evidence of the effects of wind turbine farms on AD radars," Air Warfare Center, Royal Air Force, UK, Aug. 12, 2005.
4. "Report to the congressional defense committees on the effect of windmill farms on military readiness," Office of the Director of Defense Research and Engineering, Undersecretary for Space and Sensor Systems, Aug. 2006.
5. Lemmon, J. J., J. E. Carroll, F. H. Sanders, and D. Turner, "Assessment of the effects of wind turbines on air traffic control radars," NTIA Technical Report TR-08-454, US Department of Commerce, Jul. 2008.
6. Sandifer, J. B., T. Crum, E. Ciardi, and R. Guenther, "A way forward: Wind farm — Weather radar coexistence," *Proc. WINDPOWER 2009*, Chicago, IL, May 2009.
7. Belmonte, A. and X. Fabregas, "Analysis of wind turbines blockage on doppler weather radar beams," *IEEE Antennas Wireless Propagat. Lett.*, Vol. 9, 670–673, 2010.
8. Borely, M., "Guidelines on how to assess the potential impact of wind turbines on surveillance sensors," Tech. Rep. EUROCONTROL-GUID-130, EUROCONTROL, 2010.
9. Poupart, G. J., "Wind farms impact on radar aviation interests," Final Report, Department of Trade and Industry, QinetiQ Corp., UK, Sep. 2003.
10. Kent, B. M., A. Buterbaugh, K. C. Hill, G. Zelinski, R. Hawley, L. Cravens, T. Van, C. Vogel, and T. Coveyou, "Dynamic radar

- cross section and radar Doppler measurements of commercial General Electric windmill power turbines Part 1 — Predicted and measured radar signatures,” *IEEE Antennas Propag. Mag.*, Vol. 50, No. 2, 211–219, Apr. 2008.
11. Kent, B. M., A. Buterbaugh, K. C. Hill, G. Zelinski, R. Hawley, L. Cravens, T. Van, C. Vogel, and T. Coveyou, “Dynamic radar cross section and radar Doppler measurements of commercial General Electric windmill power turbines Part 2 — Predicted and measured Doppler signatures,” *Proc. 2007 AMTA Symposium*, St. Louis, MO, 2007.
 12. Hill, K. C., G. Zelinski, T. Van, and C. Vogel, “Computational electromagnetics (CEM) prediction of a windmill,” *2007 Electromagnetics Code Consortium Annual Meeting*, May 2007.
 13. Isom, B. M., R. D. Palmer, G. S. Secrest, R. D. Rhoton, D. Saxion, T. L. Allmon, J. Reed, T. Crum, and R. Vogt, “Detailed observations of wind turbine clutter with scanning weather radars,” *J. Atmosph. Ocean. Tech.*, Vol. 26, 894–910, May 2009.
 14. Naqvi, A., S. Yang, and H. Ling, “Investigation of Doppler features from wind turbine scattering,” *IEEE Antennas Wireless Propagat. Lett.*, Vol. 9, 485–488, 2010.
 15. Greving, G., W. Biermann, and R. Mundt, “Wind turbines as distorting scattering objects for radar-clutter aspects and visibility,” *Proc. Int. Radar Symp. 2010*, 1–4, Vilnius, Lithuania, Jun. 2010.
 16. Naqvi, A., N. Whitelonis, and H. Ling, “Doppler features from wind turbine scattering in the presence of ground,” *Progress In Electromagnetics Research*, Vol. 35, 1–10, 2012.
 17. Chen, V. C., F. Li, S.-S. Ho, and H. Wechsler, “Analysis of micro-Doppler signatures,” *IEE Proc. — Radar Sonar Navig.*, Vol. 150, No. 4, 271–276, Aug. 2003.
 18. Thayaparan, T., S. Abrol, E. Riseborough, L. Stankovic, D. Lamothe, and G. Duff, “Analysis of radar micro-Doppler signatures from experimental helicopter and human data,” *IET Proc. Radar Sonar Navigat.*, Vol. 1, No. 4, 289–299, Aug. 2007.
 19. Whitelonis, N., S. Yang, and H. Ling, “Application of near-field to far-field transformation to Doppler features from wind turbine scattering,” *IEEE Trans. Antennas Propagat.*, Vol. 60, No. 3, 1660–1665, Mar. 2012.
 20. Balanis, C. A., *Advanced Engineering Electromagnetics*, 314–323, Wiley, New Jersey, 1989.